

**Effect of cohesion and shear modulus on the stability of a stretched granular layer**Hector Alarcón,<sup>1</sup> Jean-Christophe Géminard,<sup>2</sup> and Francisco Melo<sup>1</sup><sup>1</sup>*Departamento de Física, Universidad de Santiago de Chile, Av. Ecuador 3493, Casilla 307, Correo 2, Santiago, Chile*<sup>2</sup>*Université de Lyon, Laboratoire de Physique, Ecole Normale Supérieure de Lyon, CNRS, UMR 5672, Laboratoire, ENS, Université, 46 Allée d'Italie, 69007 Lyon, France*

(Received 28 May 2012; published 7 December 2012)

The main mechanism of the cellular pattern which forms at the surface of a thin layer of a cohesive granular material submitted to in-plane stretching has been identified as the “strain softening” arising from the features of grain-grain interactions. We perform measurements of the strain field associated with such structures by using a correlation image technique and additionally characterize the cohesion and shear modulus of the samples. We show that for high cohesion, the layer is fragile and the surface deformation is highly nonlinear, whereas at low cohesion, a smooth and linearly growing structure is observed as a function of external stretching. Analysis of the wavelength as a function of cohesion along with independent measurement of the shear modulus indicate that a simple model of strain softening is acceptable if a mechanism of cluster formation due to cohesion is taking place.

DOI: [10.1103/PhysRevE.86.061303](https://doi.org/10.1103/PhysRevE.86.061303)

PACS number(s): 89.75.Kd, 83.60.Uv, 45.70.Qj

**I. INTRODUCTION**

Wet granular materials are characterized by a network of liquid bonds inducing attractive capillary forces between particles [1,2]. Depending on the liquid content, several regimes are identified leading to different scalings for the cohesion force [2,3]. A relevant feature, nearly independent of the liquid content, is the “strain softening” due to both a decrease of the associated adhesion force when a single bridge elongates [4] and a decrease in the overall number of bridges which collapse when excessively stretched [5]. This effect can be seen as responsible for the relatively low plasticity of cohesive granular materials under tension, and it provides some clues as to why structures made of moist sand, such as sand castles, generally break apart in a catastrophic manner. In practice, the softening behavior is observed above a critical strain which is associated with the initial compression of the grains induced by the suction force due to the capillary bridges [6].

In a recent article [7], we explored the response of a horizontal thin layer of cohesive material to the simplest mode of deformation. An extensible membrane provided a suitable system to introduce an overall homogeneous deformation on the layer. It was shown that “strain softening” was responsible for the nearly periodic structure that develops, modulating the strain field in the layer along the pulling axis, as soon as the external deformation was turned on. The measured wavelength of the structure turned out to be linearly dependent on the layer thickness, almost independent of particle size, and a linear function of the relative humidity. The fracturing of a cohesive granular layer subjected to flexural deformation, investigated recently [8], has shown similar features.

In the present paper, we explore further “strain softening” as a mechanism of mechanical instability in a cohesive layer. We present measurements, obtained from an image-correlation technique, of the strain field associated with the cellular instability, and we characterize the cohesion and the shear modulus of the samples.

Image correlation analysis makes it possible to show that two distinct regimes of layer response appear as a function

of the cohesion. For high cohesion, the surface deformation is highly nonlinear, whereas at low cohesion a smooth and linearly growing structure is observed as a function of the external stretching. With the goal of establishing a more fundamental connection between the layer structure and the properties of the granular material, we develop experimental methods for the assessment of the cohesion and shear modulus as a function of the particle diameter and the relative humidity.

The analysis reported in Ref. [7] indicated that the wavelength  $\lambda$  increases with relative humidity, and thus with cohesion, for a given grain size but, surprisingly, that  $\lambda$  is nearly independent of the particle diameter at a given relative humidity, even if smaller grains are more cohesive in the sense that they exhibit a larger angle of avalanche.

In Ref. [7], the results were reported in terms of the relative humidity or the angle of avalanche, as the mechanical properties of the material, especially the cohesion, were not measured. In the present paper, the cohesion and the shear modulus are directly measured and the instability is analyzed in terms of the latter mechanical characteristics of the granular material. Our measurements indicate that the simple model of strain softening proposed in Ref. [7] is acceptable if a mechanism of cluster formation due to cohesion is at play.

**II. EXPERIMENTAL SETUP AND PROTOCOLS**

The experiment consists of imposing an in-plane deformation at the base of a thin layer of a cohesive granular material. To do so, the grains are initially spread onto an elastic membrane upon which the deformation is imposed (Fig. 1). The experimental setup used here is somewhat of an improvement with respect to that described in Ref. [7]. A cross is cut from a thin latex membrane (thickness 0.5 mm, width 40 cm) and is maintained at its four ends by four horizontally movable jaws. In the central part of the setup, the membrane leans on a steady, horizontal square table (width 10 cm). By displacing the jaws, whose movement can be prescribed independently by four computer-controlled motors (Thorlabs Z825BV), a wide variety of planar deformations can be achieved. For the experiments described here, the jaws are

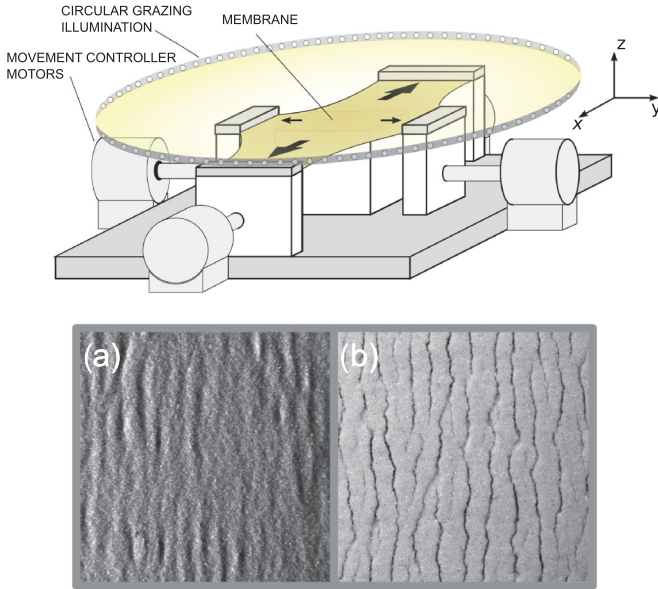


FIG. 1. (Color online) Sketch of the experimental setup. Each of the four arms of the cross-shaped membrane is independently driven by a computer-controlled motor so that a wide range of deformation modes can be achieved. For the reported experiments, uniaxial strain is achieved to better than 1% over a surface area of  $50 \text{ cm}^2$ . Lower panels: Typical cellular structures for two distinct values of the cohesion. (a) Low cohesion:  $\sigma_s = 1 \text{ Pa}$ . (b) High cohesion:  $\sigma_s = 4.1 \text{ Pa}$  ( $h = 3 \text{ mm}$ ,  $d = 53\text{--}75 \text{ }\mu\text{m}$ , and overall imposed stretching  $\theta = 0.15$ ).

controlled such that the membrane, which remains in the same horizontal plane above the table, extends along one axis but does not narrow in the perpendicular direction. We checked, using a correlation image technique described below, that the resulting overall strain field is homogeneous in the test region. As a result, the granular pattern is aligned perpendicular to the pulling direction.

The granular material consists of spherical glass beads (USF Matrasur, sodosilicate glass). We will report results obtained for various samples in a large range of bead diameters  $d$  (0–45, 53–75, 106–125, and 150–200  $\mu\text{m}$ ). Prior to each mechanical test, grains were cleaned to remove organic material and moisture. The mechanical properties of the granular matter put in contact with a humid atmosphere are likely to change with time (aging) [9,10]. To ensure that they reached a nearly stationary state, the samples were kept in contact with the desired humidity environment for 1 h prior to the experiments.

The mechanical properties of the cohesive granular material are assessed independently in two additional experiments. The cohesion is characterized by the tensile stress,  $\sigma_s$ , which is the force per unit surface one must apply to separate the material in two parts. In Ref. [7], the cohesion was indirectly accounted for by measurements of the avalanche angle,  $\theta_a$ . However, the functional relation between  $\sigma_s$  and  $\theta_a$  is complex and requires a previous calibration [9]. With the goal of measuring cohesion directly, we designed an experimental configuration to assess the pulling force that arises when a suitable indenter is pulled apart from the surface of the granular sample. In Sec. III A, the cohesion is obtained as the ratio of the maximum pulling

force to the indenter section. In the theoretical approach, the second important parameter to compare the weakening to is the shear modulus. We report in Sec. III B direct measurements of the shear modulus  $G$  as a function of cohesion in a range of normal stress which compares with the experimental conditions encountered in the tensile experiments.

In the tensile experiments, the sample is prepared first by pouring clean dry grains onto the membrane. The surface of the material is then leveled by means of a cylindrical rod guided by lateral spacers, which achieves a well-defined thickness  $h$  (from 1 to 10 mm, to within 0.1 mm). To tune the cohesion, the whole experimental device is placed in a chamber at constant humidity. The atmosphere is equilibrated with saturated salt solutions, and the relative humidity is monitored by means of a humidity meter (Lutron HT-3015). Unless specified, samples are aged during 1 h at constant humidity prior to imposing the deformation.

The free surface of the sample is imaged from above by means of a digital camera (Nikon DMX1200). A ring light source (home-made arrays of LEDs, Fig. 1) located around the elastic band, a few centimeters above the table plane, provides a good contrast. Quantitative information is obtained by extracting the flow fields using an image cross-correlation technique. To assess nonuniform flow fields (we shall see that a cellular instability indeed develops), we define a sliding window that scans the whole image, and we measure the local flow. The method gives a direct measure of the displacement field if interpreted as the average displacement of the cluster of beads enclosed by one subimage corresponding to the actual position of the sliding window. The size of the sliding window was approximately  $1 \text{ mm}^2$  (containing about 100 particles) and moved at regular horizontal and vertical increments of 0.25 mm. The spacial resolution of the method is better than 1 mm and the strain sensitivity is of about 1  $m$ strain.

### III. RESULTS

#### A. Cohesion assessment

To characterize the cohesion, we measure the force needed to pull a flat indenter apart from the free surface of the granular sample, as depicted Fig. 2. The indenter surface is coated with a layer of grains identical to those of the granular sample to be analyzed.

The indenter is first gently positioned in contact with the sample surface, and the contact force (pushing force) is monitored by a sensitive enough analytical balance (Scaltec SBA33, 100  $\mu\text{g}$  resolution). The initial pushing force is fixed at the same constant value for all samples. A computer-controlled rotation stage (Thorlabs CR1/MZ6) ensures a smooth approach and retraction of the indenter from the sample. As a check of repeatability, we report in Fig. 2(b) several behaviors of the retraction forces as a function of the upward displacement of the indenter performed under nearly equal conditions. All curves present common features when the indenter is pulled back; first the weight on the balance quickly decreases, reaches a minimum, and smoothly increases to reach a plateau. The force plateau is reached when capillary bridges are broken and the indenter is no longer in contact with the sample. Thus, we identify the force difference between

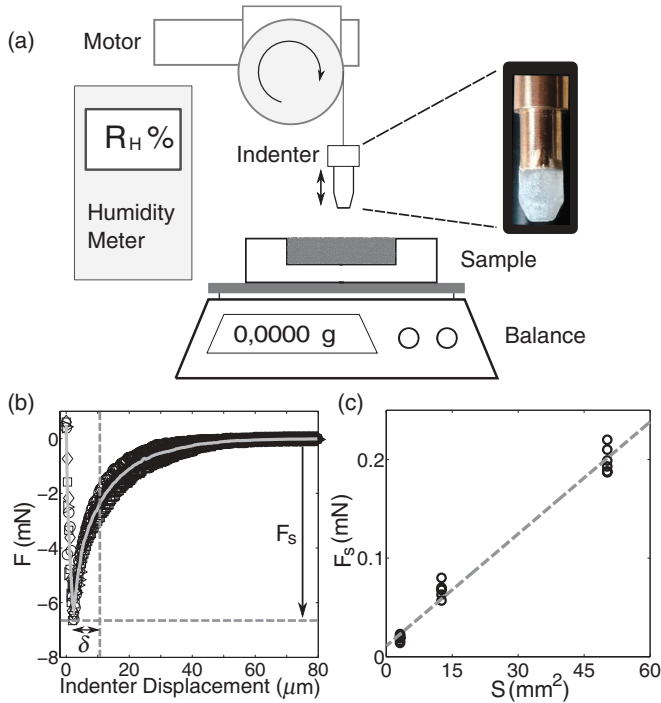


FIG. 2. (Color online) Cohesion assessment. (a) The force of cohesion  $F_s$  is measured by means of the analytical balance when the indenter is retracted at constant speed from the surface. The whole is inside a chamber at constant humidity. (b) Several retraction curves: each curve showing a minimum ( $F_s$ ) and a plateau after complete indenter retraction. Dashed line indicates the averaged force for indenter diameter 7.4 mm. (c) Cohesion force,  $F_s$ , vs indenter surface area,  $S$ .

the minimum force and the plateau as the maximum pulling force,  $F_s$ , and the typical displacement  $\delta$  for the contact loss as a measure of a critical deformation for the rupture of the material. (Notice that, given the small values of the cohesive forces and the stiffness of the scale, the displacement of the sensitive part of the balance can be neglected with respect to that of the indenter.) We consider that  $F_s$  is related to the tensile stress  $\sigma_s$  according to  $F_s = \sigma_s S$ , where  $S$  is the surface area of the contact between the indenter and the granular layer. Different surface areas were tested. The results reported in Fig. 2(c) corroborate the linear dependence of  $F_s$  on  $S$  and, thus, validate the measurements of  $\sigma_s$ .

We report in Fig. 3 the tensile stress  $\sigma_s$  as a function of the particle size  $d$  for various relative humidities  $R_H$ . Each point in the graph corresponds to the average of seven retraction trials. The dispersion in  $\sigma_s$  is of about 5%, the largest for the smallest  $R_H$ . The tensile stress  $\sigma_s$  decreases quickly when the particle size is increased, the decrease being faster for the larger humidity.

The rupture distance  $\delta$  (Fig. 4) is also extracted from the retraction force curves by assuming an exponential dependence of the pulling force on the indenter displacement. Within the experimental errors,  $\delta$  is almost independent of the particle size but is an increasing function of relative humidity. By plotting  $\delta$  versus  $\sigma_s$  (since cohesion is a more natural variable in our experiment) for a given particle size, we observe that  $\delta$  scales roughly as  $\delta \approx d^2 \sigma_s / \gamma_f$ , where the experimental constant,

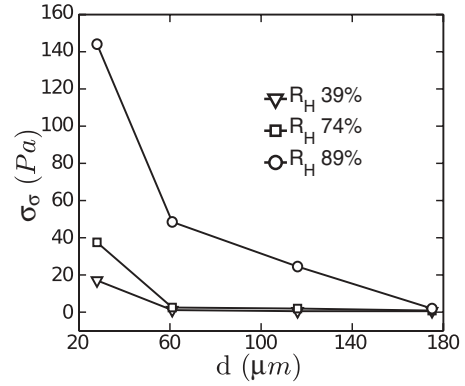


FIG. 3. Tensile stress  $\sigma_s$  vs grain size  $d$  for distinct relative humidity  $R_H$  (after 1 h of aging).

which has the dimension of a surface energy, is  $\gamma_f \approx 10 \text{ mJ/m}^2$  (Fig. 4, inset).

We notice that in our experiments, the water content is small even at relatively large humidity and that the measured tensile stress is small compared to that expected for a fully developed bridges regime ( $\sigma_s \ll \pi \gamma / d$ ) [3], which suggests that particle roughness is playing an important role in the cohesion observed here. Thus,  $\sigma_s$  scales roughly as  $1/d^2$  instead of  $1/d$ , as would occur in the regime of fully developed capillary bridges. Formally, the fully developed bridge regime should be obtained when  $\delta$  tends to be of the order of  $d$ . Interestingly,  $\delta$  is identified as being proportional to both the number of active sites (for water nucleation) and their average radius of curvature. This identification is obtained by a simple inspection of the expression for the capillary force [see Eq. (6) in Ref. [11] for details] derived in the roughness regime presented in Refs. [9,11].

To provide some additional clues for the understanding of the mechanical behavior of our samples, we assessed the typical roughness of particles through an analysis of atomic force images of the particle surfaces (Fig. 5). Scales of typical height  $l_R$  and typical width  $l_W$  of the roughness are extracted from the images by filtering the asperities, which were typically less than a few nanometers. Table I summarizes our findings, which indicate that  $l_R$  and  $l_W$  do not systematically depend on the particle size,  $d$ .

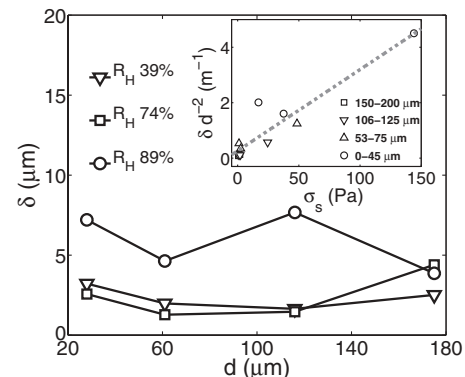


FIG. 4. Rupture distance  $\delta$  vs particle size  $d$  for distinct values of  $R_H$ . Inset:  $\delta$  as function of  $\sigma_s$  for several values of  $d$ .

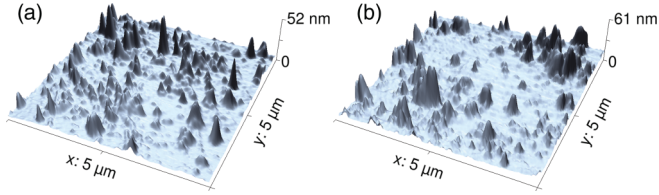


FIG. 5. (Color online) AFM images of the particle surface. (a) Particle size,  $d = 53\text{--}75\ \mu\text{m}$ . (b)  $d = 106\text{--}125\ \mu\text{m}$ .

For the purposes of the present study, we limit ourselves to the results presented above. A detailed analysis of the dependence of the cohesion on the experimental parameters, such as the particles roughness, the particle size, and the water content, will be given elsewhere.

### B. Shear modulus assessment

To characterize the shear modulus  $G$ , a Rheometer Anton Paar MCR-301 is used. It applies controlled shear stress and normal force to the sample (Fig. 6).

It is important to discuss the range of normal stress we use for this study. We are interested in the shear modulus at low confinement pressure. Indeed, given that the height of the layers is less than  $h = 0.5\ \text{cm}$ , and that the layer density is of about  $10^3\ \text{Kg/m}^3$ , the maximum pressure at the layer base is less than  $50\ \text{Pa}$ , thus of the same order as the tensile stress due to moisture.

For the test, we build samples having the shape of a circular annulus with a rectangular cross section as illustrated in Fig. 6. Sandpaper is glued to the upper and lower surfaces to avoid slippage. To ensure reliable measurements, the applied shear stress and the resulting shear deformation in the whole sample thickness are measured independently. To do so, we analyze images of the layer taken from the side (Fig. 6). Image correlation analysis is used to obtain the shear field on a squared window of the sample. By plotting the shear stress against the shear strain, for given normal forces  $P_n$ , we obtain  $G$  for various humidity conditions.

Due to the necessity of building annular self-standing samples, only small particles which are cohesive enough are tested,  $d = 30\ \mu\text{m}$ ; small particles with the highest cohesion allow us to scan a relatively wide range of  $R_H$ . In turn, larger particles, at low humidity, exhibit low cohesion, which makes the samples less stable when the normal force is increased. Measurements of the tensile stress are carried out in the same samples as soon as the shear test concludes to avoid aging errors.

We report the shear modulus  $G$  as a function of the applied normal stress  $P_n$  for distinct values of the cohesion in Fig. 7. We notice that when  $G$  is plotted against  $\sigma_s + P_n$ , all results collapse in a single straight line, which indicates that the proper confinement pressure includes the additional contribution of the cohesion. This result is particularly interesting and deserves

TABLE I. Typical lengths  $l_R$  and  $l_W$ .

$d\ (\mu\text{m})$	0–45	53–75	105–125	150–200
$l_R\ (\text{nm})$	70	50	100	70
$l_W\ (\text{nm})$	270	365	680	460

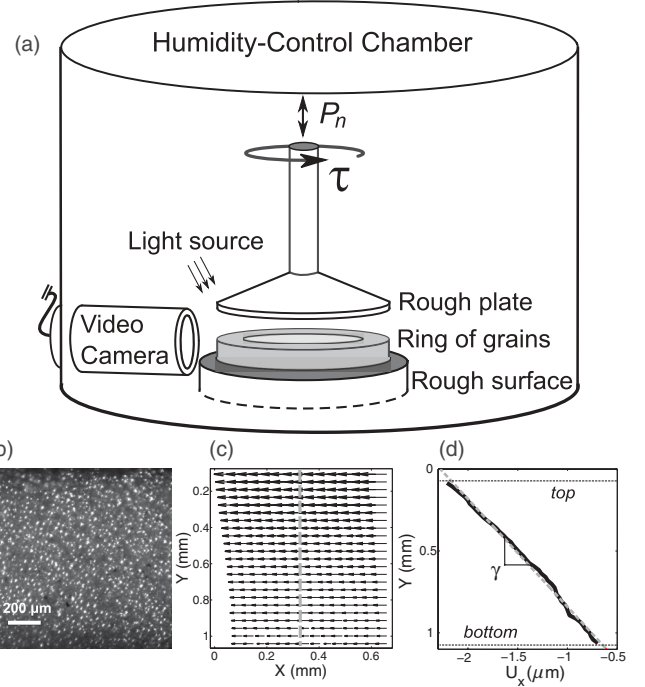


FIG. 6. (Color online) Shear modulus measurements. (a) Sketch of the setup. The sample is a ring of internal diameter  $18\ \text{mm}$  and of rectangular cross section of  $4\ \text{mm}$  in width by  $1\ \text{mm}$  in height. (b) Image from the side of the granular sample. (c) Displacement field; arrows indicate the grain displacement obtained by means of correlation analysis. (d) Displacement profile. Horizontal lines indicate the top and bottom boundaries of the shear cell.

to be thoroughly discussed. For spheres interacting through a Hertz potential,  $G$  would scale as  $P_n^{1/3}$ . In turn, for a highly cohesive ensemble of Hertzian spheres, it has been recently shown [12] that  $G \sim E^{2/3}(\sigma_s + P_n)^{1/3}$ , where  $E$  is the bulk modulus of the material. In our case, the linear dependence of  $G$  on  $P_n$  and the relative low values of the cohesion suggest that a different kind of elastic interaction is taking place. Let us consider that the contact between the spherical grains is dominated by rugosities or even asperities of typical size scale  $l_R$ . In this case,  $F_s + N_n = J A_r$ , where  $F_s$  and  $N_n$  are the

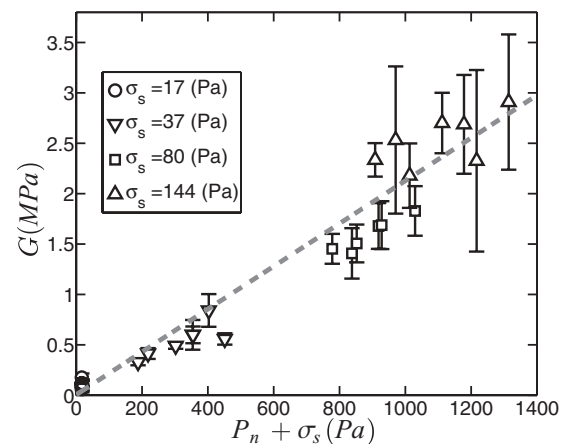


FIG. 7. Shear modulus  $G$  vs  $\sigma_s + P_n$  for various cohesions ( $d = 0\text{--}45\ \mu\text{m}$ ).

capillary force and the applied normal force, respectively,  $J$  is the yield stress of the material, and  $A_r$  is the real area of contact. Consistently, for roughness-dominated contacts, the elastic force exhibits a linear dependence on the local strain,  $\delta/l_R$ , so that  $F_{el} \approx EA_r \Delta \delta / l_R$ . Considering that the shear modulus differs from the effective bulk modulus  $E_{eff} \propto (F_{el}/d^2)/(\Delta \delta/d)$  only by a factor of the order of unity [13] and including the geometric factor [12], we find

$$G \approx \frac{Ed}{6Jl_R}(\sigma_s + P_n). \quad (1)$$

From experimental data, we obtain  $E/(Jl_R) \approx 6 \times 10^8$  m. For  $l_R \approx 100$  nm, a value that is obtained by measuring the spheres roughness from atomic force microscopy (AFM) images, the ratio  $E/J$  is estimated to be about 40, which is an acceptable value. Indeed, independent measurements for a sodosilicate glass provide typical values of  $E \approx 70$  GPa and  $J \approx 3$  GPa, which gives  $E/J \approx 25$  [14]. In addition, in experiments of indentation on a plate of soda-lime-silica-glass, a current value is  $E/J \approx 40$  [15]. On the other hand, as a check of consistency, it is interesting to ask for the fraction  $\psi$  of contacts that are actually acting in the plastic regime with respect to the elastic ones, as given by the well-known Greenwood-Williamson approach [16]. This is  $\psi \equiv (l_R/\rho)^{1/2} E/J$ , where  $\rho$  is the curvature radius of typical asperities, which is approximated to  $\rho \approx l_W^2/8l_R$ . With the data in Table I and taking  $E/J \approx 40$ , we find that  $\psi \approx 20$ , which is consistent with our hypothesis of plastified contacts.

### C. Pattern characterization

When the membrane is stretched by imposing the homogeneous strain field of amplitude  $\theta \equiv U_{xx}$  at the base of the granular layer, one observes, provided that the grains are small enough and/or the relative humidity  $R_H$  is large enough, the growth of a rather regular pattern at the free surface (Fig. 1). Domains, made of stripes having a rather well-defined width and making a straight angle with the stretching direction ( $x$  axis, Fig. 1), nucleate and grow.

Figure 8 presents the modulation of the displacement fields along the pulling direction (the imposed deformation is subtracted from the measured displacement field). For the case of low cohesion, presented in the uppermost panels, even if the structure is barely visible from the pictures, image correlation analysis reveals a small modulation whose amplitude increases with  $\theta$ . We point out that as  $\theta$  is increased, the pattern evolves toward a structure of a relatively well selected wavelength. The right panels in Fig. 8 include the displacement  $U_x - \theta x$  and its respective strain  $dU_x/dx - \theta$  along a selected line (dashed lines) parallel to the pulling direction. The strain varies smoothly.

In contrast, for relatively high cohesion (Fig. 8, lowermost panels), a rather well-defined wavelength is observed, even at small stretching  $\theta$ . Displacement and strain profiles indicate a nonlinear behavior from the early stages of the structure development. Large positive strains are localized, whereas an extended region that is poorly stretched can be observed. As a consequence, when the stretching is increased further, the structure develops with a continuous increase of the strain in

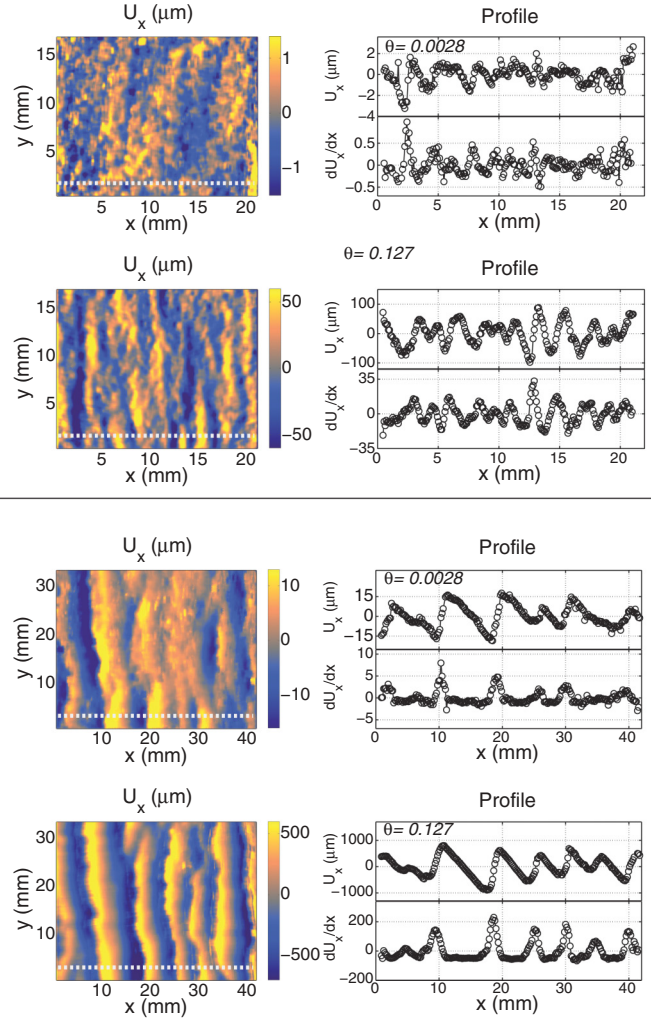


FIG. 8. (Color online) Displacement fields for two distinct values of cohesion at a given thickness. Left: Modulation of the displacement fields  $U_x(x, y) - \theta x$ . Right: Profiles of the modulation  $U_x(x) - \theta x$  and associated modulation of the strain  $dU_x/dx - \theta$  (in  $mstrain$ ) measured along the dashed lines. Results are reported for low cohesion,  $\sigma_s = 1$  Pa (uppermost panel), and relatively high cohesion,  $\sigma_s = 10$  Pa (lowermost panel), and for two values of the imposed stretching,  $\theta = 0.0028$  and  $0.127$ , as indicated in the panels ( $h = 5$  mm,  $d = 53\text{--}75$   $\mu\text{m}$ ).

localized regions, which leads to the fracture of the granular layer in these regions of focused dilations.

From now on, it will be particularly interesting to consider the dependence of the amplitude  $A$  of the displacement-field modulation at the free surface as a function of the average strain imposed at the base plane,  $\theta$ . The sensitivity of the image correlation method makes it possible to accurately determine the rms amplitude (normalized to the average wavelength),  $A/\lambda$ , as a function of  $\theta$  (Fig. 9). One observes that the amplitude of the modulation starts growing linearly with  $\theta$  as soon as the layer is stretched. Confirming with a much better accuracy a result obtained in Ref. [7], these experiments prove that the instability does not exhibit any significant threshold in terms of deformation.

At this point, we consider the dependency of the typical wavelength,  $\lambda$ , of the fracture pattern on the cohesion. We first

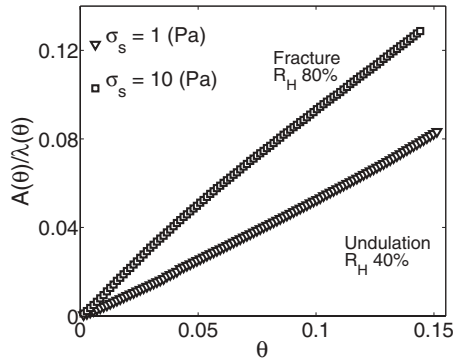


FIG. 9. rms amplitude of the strain variation along the stretching direction (same conditions as those in Fig. 8).

mention that  $\lambda$  is not strictly selected and that a large scatter on the stripes width is observed. In spite of the scatter, we observe that  $\lambda \propto h$  on average. In Ref. [7],  $\lambda$  was observed to be almost independent of  $d$  for a given relative humidity,  $R_H$ , and thickness,  $h$ . Here, our image analysis method allows the assessment of the wavelength at very low cohesion for much lower imposed external displacement, which in turn minimizes scatter of the measurements. Figure 10 presents the wavelength of the structure as a function of relative humidity,  $R_H$ , as well as cohesion, accounted for by the tensile stress  $\sigma_s$ . For small  $R_H$ ,  $\lambda$  is nearly independent of  $R_H$ , but it strongly increases when  $R_H$  reaches a value about 70% (note that such a relative humidity is typical of the transition between the roughness and the smooth-sphere regimes for the capillary bridges [3]). However, when  $\lambda$  is plotted against  $\sigma_s$ , only a slow increase is observed. Interestingly, when  $\sigma_s$  is used as an independent variable instead of  $R_H$ , a small but significant dependence of  $\lambda$  on the particle size,  $d$ , is revealed. In addition, at vanishing cohesion,  $\lambda \approx 0.6h$  independently of  $d$ .

#### IV. THEORETICAL ANALYSIS

In the following, we remind the reader of the main ideas presented in Ref. [7] regarding the mechanism of pattern formation on the cohesive layer. As observed in Sec. III A, due to the capillary nature of the interaction between the grains, the cohesion force decreases when the material is stretched and, thus, grains are pulled apart [5,6]. When the membrane is elongated, a homogeneous stretching of the

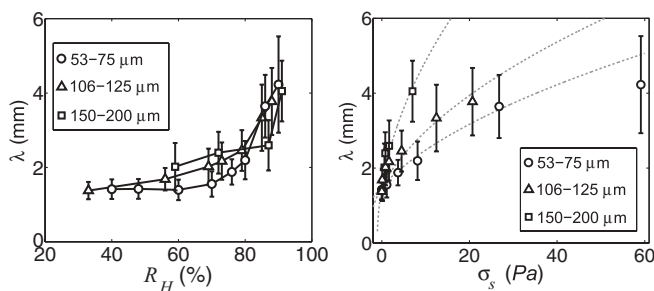


FIG. 10. Left: Wavelength  $\lambda$  vs relative humidity  $R_H$ . Right: Same vs tensile stress  $\sigma_s$ . Dashed lines are the best fit to  $\lambda$  obtained by using Eq. (6) with  $\beta = (0.44 \pm 0.03) \text{ mJ/m}^2$ . For  $h = 3 \text{ mm}$  and  $d = 53\text{--}75, 106\text{--}125, \text{ and } 150\text{--}200 \text{ }\mu\text{m}$ .

material is imposed in the base plane. However, due to the “strain softening,” in response to the overall stretch, the layer tends spontaneously to modulate the deformation. Indeed, regions of large deformation are associated with a smaller tensile modulus (cohesion), and regions of large modulus are associated with a smaller deformation, which results in an overall decrease of the energetic cost. Simultaneously, the modulation induces a shear deformation which is associated with an energetic cost. Thus, it is expected that the wavelength is governed by the balance of the gain associated with the modulation of the horizontal strain and the loss associated with the resulting shear. To account for the experimental observations, let us first assume that the normal stress along the  $x$  axis,  $\sigma_{xx}$ , decreases linearly with the uniaxial strain  $u_{xx}$  according to  $\sigma_{xx} = \sigma_s(1 - u_{xx}/\theta_m)$  when the material is stretched ( $u_{xx} > 0$ ) [6]. The relation is no longer valid for  $u_{xx} > \theta_m$ , when the elongation is large enough for the bridges to collapse and, thus, for the material to break apart. Thus,  $\theta_m$  represents the typical strain for which a significant softening occurs, whereas  $\sigma_s$  denotes the tensile stress prior to deformation. For the sake of simplicity, the contribution of the shear will be accounted for by a simple shear modulus  $G$  whose value will be discussed later. In this framework, the shear stress  $\sigma_{xz} = Gu_{xz}$  and, accordingly, the energy per unit volume

$$E = \sigma_s \left( u_{xx} - \frac{u_{xx}^2}{2\theta_m} \right) + \frac{1}{2} Gu_{xz}^2. \quad (2)$$

A sinusoidal perturbation of the displacement such that  $u_x = \theta x + f(z) \sin(kx)$  in the horizontal plane is considered, and, to obtain the associated displacement in the vertical direction  $u_z$ , dilation is neglected,  $u_{xx} + u_{zz} = 0$ . The wavelength  $\lambda \equiv 2\pi/k$  is thus found to be proportional to  $h$ , independent of  $\theta$ , according to  $\lambda = 2\pi \frac{\sqrt{1+\xi}}{\arccos(-1/\xi)} h$ , provided that  $\xi \geq 1$ , where  $\xi \equiv 2\sigma_s/(G\theta_m)$ . Thus, the layer is always unstable provided that the decrease in the tensile stress is large enough compared to the shear counterpart, i.e.,  $\frac{\sigma_s}{\theta_m} \geq \frac{G}{2}$ .

The growth of the instability is limited by the condition that  $u_{xx}(x, h) \geq 0$  for all  $x$  at the free surface, and the amplitude of the vertical displacement,  $ka$ , is predicted to be proportional to  $\theta h$ .

#### V. DISCUSSION

Interestingly, the theoretical analysis, which involves both a decrease of the tensile stress associated with the stretching of the material and an energetic cost associated with the induced shear, predicts that a stretched layer is always unstable. In agreement with the experimental observations, the instability does not exhibit any finite threshold, and the amplitude of the modulation increases linearly with  $\theta$  (Fig. 9).

One important point is that the effect of the humidity content on the wavelength is accounted for by the dependence of  $\lambda$  on the ratio  $\xi \equiv 2\sigma_s/(G\theta_m)$ . For instance, in the limit of large  $\xi$  (small bridges), one expects

$$\lambda \simeq 4\sqrt{2\sigma_s/G\theta_m} h. \quad (3)$$

As discussed in Ref. [7], the experimental increase of  $\lambda$  with  $R_H$  would impose, in the framework of the simplified model,

that  $G$  increases more slowly than the ratio  $\sigma_s/\theta_m$ . Note that  $\sigma_s$  and  $\theta_m$  both should increase with  $R_H$ .

In light of the measurements presented in Sec. III B, the shear modulus  $G$  is indeed a linear function of  $\sigma_s$ . We obtained  $G \approx (\sigma_s + P_n)Ed/6Jl_R$ , which when replaced in Eq. (3) leads to

$$\lambda \simeq 4\sqrt{12\sigma_s J l_R / Ed\theta_m(\sigma_s + P_n)h}. \quad (4)$$

Notice that, at the thicknesses explored in our experimental conditions, the pressure due to the grain weight at the base of the layer,  $P_n \approx \rho gh$ , is in most cases much smaller than  $\sigma_s$ , which allows us to neglect  $P_n$  for small  $h$  and sufficiently high  $\sigma_s$ . Thus, the dependence of  $\lambda$  on  $\sigma_s$  vanishes, indicating that the origin of the dependence of the wavelength on the humidity is not likely through the variables discussed up to now. We notice that the only remaining quantity which depends on  $R_H$  is  $\theta_m$ . It is then natural to take  $\theta_m$  as the typical strain necessary for rupture, i.e., the ratio of the typical elongation for rupture  $\delta_s$  to the typical size of the object that is stretched,  $L_c$ . Given the small water content in the system, it is reasonable to take  $\delta_s$  as the typical size of the asperities,  $l_R$ . In addition, the water is likely to be heterogeneously distributed in the system and, thus, the grains are likely to form wet clusters [2,17]. To account for the clustering, we assume that  $L_c \approx \alpha_s d/2$ , where  $\alpha_s$  is the typical size expressed in the number of grains of a typical cluster in the system. With these assumptions, we get

$$\lambda \simeq 4\sqrt{6J\alpha_s/Eh}. \quad (5)$$

Finally, in order to account for the whole dependence of  $\lambda$  on the humidity, a guess for the dependence of the size of the clusters on the cohesion is necessary. Noticing that  $\alpha_s$  must tend to 1 for vanishing  $\sigma_s$  and should be an increasing function of  $\sigma_s$ , we then write  $\alpha_s \approx 1 + \sigma_s d^2/\beta l_R$ , where  $\beta$  is a constant with the dimension of surface energy. The latter choice, which

is motivated by the dependence of the elongation distance before rupture,  $\delta$ , observed in the indenter experiment reported in Sec. III A, correctly describes the functional dependence of  $\lambda$  on both  $\sigma_s$  and  $d$ . Indeed, the final expression

$$\lambda \simeq 4\sqrt{6J(1 + \sigma_s d^2/\beta l_R)/Eh} \quad (6)$$

predicts that, in the limit of small  $\sigma_s$ , independently of the choice for the scaling for clustering formation,  $\lambda \approx 4\sqrt{6J/Eh}$ . Experimentally, we obtain  $\lambda \approx 0.6h$ , which predicts that  $E/J \approx 200$ , which is of the same order but significantly larger than that obtained from shear modulus measurements (see Sec. III B). Solid lines in Fig. 10 correspond to the best fit to  $\lambda$  using the values of  $l_R$  given in Table 1 and the constant  $\beta$  as a unique free parameter. We get  $\beta = (0.44 \pm 0.03) \text{ mJ/m}^2$ . This value indicates that cluster size ranges from  $d$  to  $10d$ .

## VI. CONCLUSIONS

In conclusion, we have presented measurements of the strain field associated with the instability of a stretched cohesive granular layer obtained by image correlation analysis. The wavelength of the structure is an increasing function of both the cohesion and the particle diameter. The ‘‘strain softening mechanism’’ proposed in Ref. [7], along with measurements of tensile strength and shear modulus, lead us to hypothesize that a clustering effect might be at play.

## ACKNOWLEDGMENTS

The authors acknowledge the financial support from the contracts ANR-CONICYT 011 (ANR-09-BLAN-0389-01) and anillo ACT95. The authors also would like to thank an anonymous reviewer for his contribution to the final discussion of our findings.

- 
- [1] Z. Fournier *et al.*, *J. Phys.: Condens. Matter* **17**, S477 (2005).
  - [2] M. Scheel, R. Seemann, M. Brinkmann, M. Di Michiel, A. Sheppard, B. Breidenbach, and S. Herminghaus, *Nature (London)* **7**, 189 (2008).
  - [3] T. C. Halsey and A. J. Levine, *Phys. Rev. Lett.* **80**, 3141 (1998).
  - [4] J. Crassous, E. Charlaix, and J. L. Loubet, *Phys. Rev. Lett.* **78**, 2425 (1997).
  - [5] C. D. Willett, M. J. Adams, S. A. Johnson, and J. P. K. Seville, *Langmuir* **16**, 9396 (2000).
  - [6] T. Gröger, U. Tüzün, and D. M. Heyes, *Powder Technol.* **133**, 203 (2003).
  - [7] H. Alarcón, O. Ramos, L. Vanel, F. Vittoz, F. Melo, and J.-C. Géminard, *Phys. Rev. Lett.* **105**, 208001 (2010).
  - [8] J.-C. Géminard, L. Champougny, P. Lidon, and F. Melo, *Phys. Rev. E* **85**, 012301 (2012).
  - [9] L. Bocquet, E. Charlaix, S. Ciliberto, and J. Crassous, *Nature (London)* **396**, 735 (1998).
  - [10] S. Nowak, A. Samadani, and A. Kudrolli, *Nat. Phys.* **1**, 50 (2005).
  - [11] L. Bocquet, E. Charlaix, and F. Restagno, *C. R. Phys.* **3**, 207 (2002).
  - [12] P. C. F Moller and D. Bonn, *Europhys. Lett.* **80**, 38002 (2007).
  - [13] L. D. Landau and E. M. Lifchitz, *Theory of Elasticity* (Pergamon, New York, 1959).
  - [14] P. Forquin and F. Hild, *Adv. Appl. Mech.* **44**, 1 (2010).
  - [15] J. T. Hagan and S. Van Der Zwaag, *J. Non-Cryst. Solids* **64**, 249 (1984).
  - [16] See, for instance, K. L. Johnson, *Contact Mechanics* (Cambridge University Press, Cambridge, 1985).
  - [17] M. Scheel, R. Seemann, M. Brinkmann, M. Di Michiel, A. Sheppard, and S. Herminghaus, *J. Phys.: Condens. Matter* **20**, 494236 (2008).